

Probing coherence in metal absorption towards multiple images of strong gravitationally lensed quasars

Rajeshwari Dutta,^{1,2,3*} Ana Acebron,^{4,5} Michele Fumagalli,^{2,6} Claudio Grillo,^{4,5} Gabriel B. Caminha,^{7,8} Matteo Fossati^{2,3}

¹ IUCAA, Postbag 4, Ganeshkind, Pune 411007, India

² Dipartimento di Fisica G. Occhialini, Università degli Studi di Milano Bicocca, Piazza della Scienza 3, 20126 Milano, Italy

³ INAF - Osservatorio Astronomico di Brera, via Bianchi 46, 23087 Merate (LC), Italy

⁴ Dipartimento di Fisica, Università degli Studi di Milano, Via Celoria 16, I-20133 Milano, Italy

⁵ INAF - IASF Milano, via A. Corti 12, I-20133 Milano, Italy

⁶ INAF - Osservatorio Astronomico di Trieste, via G. B. Tiepolo 11, I-34143 Trieste, Italy

⁷ Technical University of Munich, TUM School of Natural Sciences, Department of Physics, James-Frank-Str 1, 85748 Garching, Germany

⁸ Max-Planck-Institut für Astrophysik, Karl-Schwarzschild-Str. 1, D-85748 Garching, Germany

Accepted XXX. Received YYY; in original form ZZZ

ABSTRACT

We present a tomographic analysis of metal absorption lines arising from the circumgalactic medium (CGM) of galaxies at $z \approx 0.5$ – 2 , using Multi Unit Spectroscopic Explorer (MUSE) observations of two background quasars at $z \approx 2.2$ and 2.8 , which are two of the few currently known quasars with multiple images due to strong gravitational lensing by galaxy clusters at $z \approx 0.6$ and 0.5 , respectively. The angular separations between different pairs of quasar multiple images enable us to probe the absorption over transverse physical separations of ≈ 0.4 – 150 kpc, which are based on strong lensing models exploiting MUSE observations. The fractional difference in rest-frame equivalent width (ΔW_r) of Mg II, Fe II, C IV absorption increases on average with physical separation, indicating that the metal-enriched gaseous structures become less coherent with distance, with a likely coherence length scale of ≈ 10 kpc. However, ΔW_r for all the ions vary considerably over ≈ 0.08 – 0.9 , indicating a clumpy CGM over the full range of length scales probed. At the same time, paired Mg II absorption is detected across ≈ 100 – 150 kpc at similar line-of-sight velocities, which could be probing cool gas clouds within the same halo. No significant dependence of ΔW_r is found on the equivalent width and redshift of the absorbing gas and on the galaxy environment associated with the absorption. The high-ionization gas phase traced by C IV shows a higher degree of coherence than the low-ionization gas phase traced by Mg II, with ≈ 90 percent of C IV systems exhibiting $\Delta W_r \leq 0.5$ at separations ≤ 10 kpc compared to ≈ 50 percent of Mg II systems.

Key words: galaxies: evolution - quasars: absorption lines - galaxies: structure - gravitational lensing: strong

1 INTRODUCTION

By regulating the flow of baryons in and out of galaxies, the circumgalactic medium (CGM) plays a vital role in galaxy evolution (Tumlinson et al. 2017). On one hand, pristine gas is accreted from the large-scale structures through the CGM onto the galaxy, while on the other hand, star formation and nuclear activity in the galaxy drive metal-enriched outflows into the CGM. The expelled metals either fall back onto the galaxy or spread in the intergalactic medium. Studying the distribution and mixing of metals around galaxies is therefore crucial to understanding the star formation history and chemical enrichment of galaxies (Péroux & Howk 2020).

Due to its low density, the CGM has been most effectively probed in absorption against bright background sources such as quasars. Large surveys have statistically mapped the distribution of metal absorp-

tion lines around galaxies across different gas phases and redshifts (e.g. Tumlinson et al. 2011; Nielsen et al. 2013; Turner et al. 2014; Dutta et al. 2020, 2021; Galbiati et al. 2023). Ionization modeling of absorption line systems has been used to place constraints on the average physical conditions of the gas clouds such as metallicity, density, and size (e.g. Werk et al. 2014; Fumagalli et al. 2016; Haislmaier et al. 2021; Sameer et al. 2021; Zahedy et al. 2021; Lofthouse et al. 2023), albeit these estimates are subject to the model assumptions.

The major limitation of absorption line studies is that they probe the gas only along a pencil-beam sightline towards the background point source and hence cannot directly map the spatial distribution of the gas. In contrast, spatially resolved emission can directly map the extent and morphology of the gas around galaxies. However, due to its low surface brightness, the CGM has been challenging to detect in emission at cosmological distances. Now, thanks to sensitive integral field unit (IFU) spectrographs, such as the Multi Unit Spectroscopic Explorer (MUSE; Bacon et al. 2010) on the Very Large Telescope

* E-mail: rajeshwari.dutta@iucaa.in

(VLT), it is becoming possible to detect extended Ly α emission (e.g. Borisova et al. 2016; Leclercq et al. 2017; Arrigoni Battaia et al. 2019; Fossati et al. 2021), and metal line emission (e.g. Burchett et al. 2021; Zabl et al. 2021; Leclercq et al. 2022; Dutta et al. 2023) around galaxies, although individual detections of metal line emission from the CGM are still only a handful and limited to the inner, most dense, CGM.

Alternative approaches to study the spatial extent and coherence scale of the CGM have been to use quasar pairs, gravitationally lensed quasars and arcs, and extended background galaxies. Absorption lines detected towards close quasar pairs have been used to measure the physical extent of the metal-enriched CGM using transverse clustering analysis over hundreds of kpc (e.g. Hennawi & Prochaska 2007; Martin et al. 2010; Rubin et al. 2015; Mintz et al. 2022). Multiple images of gravitationally lensed quasars have been used to study the structure of the absorbing gas on smaller length scales of few kpc (e.g. Rauch et al. 2001; Chen et al. 2014; Zahedy et al. 2016; Rubin et al. 2018; Kulkarni et al. 2019; Augustin et al. 2021). Estimates of the coherence length scale, i.e. the length scale over which absorption does not vary significantly, from these studies suggest that the high-ionization gas phase is more coherent and spread out than the low-ionization gas phase. Recently, it has become possible to probe the absorbing gas over an extended region at sub-kpc scales using MUSE observations of background lensed arc images and extended galaxies (e.g. Lopez et al. 2018; Péroux et al. 2018; Tejos et al. 2021). These studies have found that the distribution of metals around individual galaxies is similar to that around statistical samples of galaxies, and that there are indications of metals being mixed efficiently on kpc-scales in the CGM.

However, systems in which tomographic studies can be conducted are rare, and the structure of the CGM at different length scales is still poorly constrained. It is, therefore, important to expand the sample of systems in which one can spatially map the metal-enriched gas. In this work, we study the metal absorption towards multiple images of two background quasars that are gravitationally lensed by galaxy clusters. Thanks to strong gravitational lensing (magnification ≈ 2.5 –17), the MUSE spectra of the multiple quasar images are among the ones with the largest equivalent exposure times (≈ 30 –1400 h) available to date. Unlike most lensed quasar studies that typically probe smaller physical separations ($\lesssim 20$ kpc), the angular separations (≈ 2 –22 arcsec) between the different pairs of quasar images studied here enable us to probe the absorbing gas over a wide range of physical separations, ≈ 0.4 –150 kpc. The MUSE spectroscopic observations of these two fields enable constructing an accurate lens mass model and, consequently, accurate estimates of the physical separation between quasar sightlines at the absorber redshifts. We use the Mg II and Fe II absorption lines to study the coherence of the low-ionization gas phase and the C IV absorption lines to study the coherence of the high-ionization gas phase. Furthermore, the MUSE observations of the two lensed systems allow us to study the association of metal absorption with nearby galaxies.

The paper is structured as follows. We provide a brief overview of the observations used in this work in Section 2. The results on the correlation of metal absorption lines between different quasar sightlines and on the connection with galaxies are presented in Section 3. We discuss and summarise the results in Section 4. We adopt a Flat Λ CDM cosmology with $H_0 = 70$ km s $^{-1}$ Mpc $^{-1}$ and $\Omega_M = 0.3$, and express all distances in physical units.

2 OBSERVATIONS & ANALYSIS

The fields SDSS J1029+2623 (J1029 hereafter) and SDSS J2222+2745 (J2222 hereafter) were observed with MUSE for 4.8 h and 4.4 h on target, respectively [PID: 0102.A-0642(A), 0103.A-0554(A); P.I.: C. Grillo]. The observations took place between 2019 March and July. Based on the analysis of the MUSE Analysis of Gas around Galaxies survey (Lofthouse et al. 2023), which consists of similar exposure times, we estimate the MUSE data to have a 90 percent photometric completeness limit of $r \approx 26$ mag for point sources, and a 90 percent spectroscopic flux completeness limit of $\approx 3 \times 10^{-18}$ erg s $^{-1}$ cm $^{-2}$ at 5000 Å for point sources. The data were reduced using the ESO pipeline (Weilbacher et al. 2020) following standard procedures. The sky subtraction was performed using the Zurich Atmosphere Purge (Soto et al. 2016). Further details of the data reduction are provided in Acebron et al. (2022b) and Acebron et al. (2022a). The wavelength coverage of the MUSE data is ≈ 4750 – 9350 Å, and the spectral resolution is ≈ 2000 – 3000.

The sources are detected based on the Hubble Space Telescope (HST) WFC3/F814W image using SExtractor (Bertin & Arnouts 1996). The HST observations and data reduction are described in Oguri et al. (2013) and Sharon et al. (2017). The one-dimensional spectra of the sources detected in HST were extracted from the MUSE cubes within a circular aperture of radius 0.8 arcsec, similar to the full-width at half-maximum of the point spread function. The redshifts of the sources were estimated by cross-matching the spectra with different spectral templates and emission lines. In this work, we consider the galaxies with reliable redshifts (quality flag ≥ 2 ; Acebron et al. 2022b,a).

The left panel of Fig. 1 shows the MUSE image of the field J1029. This field contains three multiple images (A, B, C) of a quasar at $z_{\text{QSO}} = 2.1992$ that is lensed by a galaxy cluster at $z_{\text{lens}} = 0.588$. The angular separation between the quasar images ranges from 1.9 to 22.5 arcsec. The MUSE spectra of the three quasar multiple images are shown in the right panel of Fig. 1.

In addition to the MUSE spectra, archival [PID: 092.B-0512(A)] UVES spectra are available for the multiple images A and B of the quasar J1029. The UVES observations were performed from 2014 January to February. The reduced UVES spectra were obtained from the ESO archive. The individual exposure spectra were combined by interpolating to a common wavelength array and weighting each flux pixel by the inverse variance. The wavelength coverage of the final spectrum is ≈ 3300 – 6600 Å, and the spectral resolution is ≈ 30000 . The UVES spectra of the quasar multiple images A and B, along with the MUSE spectra, are shown in the right panel of Fig. 1.

The field J2222 (see left panel of Fig. 2) contains six multiple images (A, B, C, D, E, F) of a background quasar at $z_{\text{QSO}} = 2.801$ that is lensed by a galaxy cluster at $z_{\text{lens}} = 0.489$. The quasar images D, E and F are contaminated by the light from nearby bright cluster members in the MUSE data, and their one-dimensional spectra cannot be utilized for an absorption line analysis. This work exploits the spectra of the quasar images A, B, and C (see right panel of Fig. 2). The angular separation between these images ranges from 4 to 15 arcsec.

All the MUSE and UVES quasar spectra were converted into the heliocentric frame and vacuum wavelength for the analysis. For the identification and analysis of absorption lines, the continuum normalisation of the quasar spectra was carried out by spline fitting using LINETOOLS. The signal-to-noise ratio per pixel of the MUSE quasar spectra ranges between ≈ 30 and ≈ 90 around 7000 Å, and that of the UVES quasar spectra is ≈ 20 around 5000 Å.

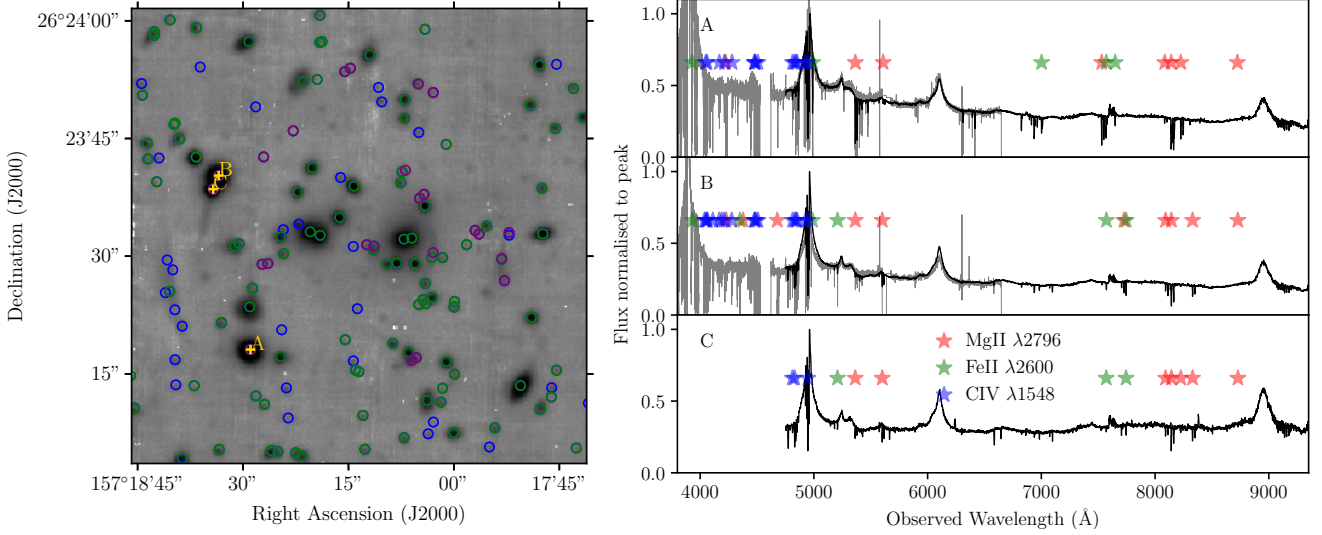


Figure 1. *Left:* MUSE white light image of the field J1029. The three multiple images, A, B, and C, of the quasar are marked with '+'. The blue circles identify all the sources detected in the HST F814W image, the green circles denote the sources that have reliable spectroscopic redshifts, and the purple circles indicate the multiple imaged sources. *Right:* Spectra of the three quasar multiple images extracted from the MUSE cube. The UVES spectra are also shown for images A and B in grey. The stars mark the Mg II λ 2796 (red), Fe II λ 2600 (green), and C IV λ 1548 (blue) absorption lines detected in the spectra.

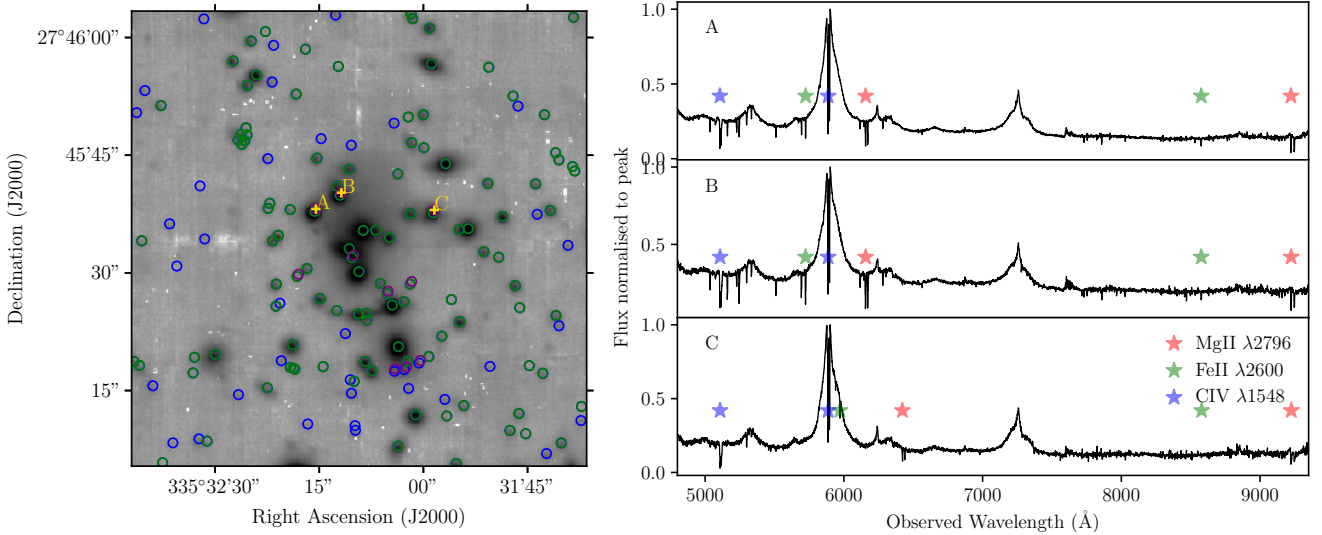


Figure 2. Same as in Fig. 1 for the field J2222.

3 RESULTS

3.1 Metal absorption across two quasar sightlines

We identified all the metal absorption lines, such as Mg II, Mg I, Fe II, C IV, and Si IV, in each of the quasar normalised spectra redward of the quasar Ly α emission line. The Mg II, Fe II, and C IV systems identified in the different quasar image spectra are listed in the appendix and also marked on top of the quasar spectra shown in the right panels of Figures 1 and 2. We estimate the optical depth-weighted median redshift and rest-frame equivalent width of the absorption lines. We note that in the case of J1029, the UVES spectra of the quasar multiple images A and B provide coverage of the Mg II and Fe II lines at the redshift of the lens cluster, $z \approx 0.588$. However, we do not detect any absorption from the cool low-ionization gas (rest equivalent width of

Mg II $\leq 0.05 \text{ \AA}$) at the redshift of the cluster. For both quasars, C IV absorption is detected at the quasar redshift towards all the multiple images. However, we do not include the intrinsic absorption in the following analysis.

For each quasar, we search for counterpart absorbers within $\pm 500 \text{ km s}^{-1}$ towards the different images. For context, the escape velocity at the virial radius for a galaxy group at $z = 1$ with halo mass, $M_h \approx 10^{13} M_\odot$, is $\approx 500 \text{ km s}^{-1}$. In most cases, the absorber pairs lie within $\pm 100 \text{ km s}^{-1}$ of each other. Some examples of absorption lines detected across the multiple quasar sightlines are shown in Fig. 3. We find 20 Mg II absorber pairs and 10 Fe II absorber pairs over $z \approx 0.5 - 2.3$, and 18 C IV absorber pairs over $z \approx 1.6 - 2.3$. For similar redshift, line-of-sight velocity window, and equivalent width limits (0.01 \AA for Mg II and 0.05 \AA for C IV), and based on

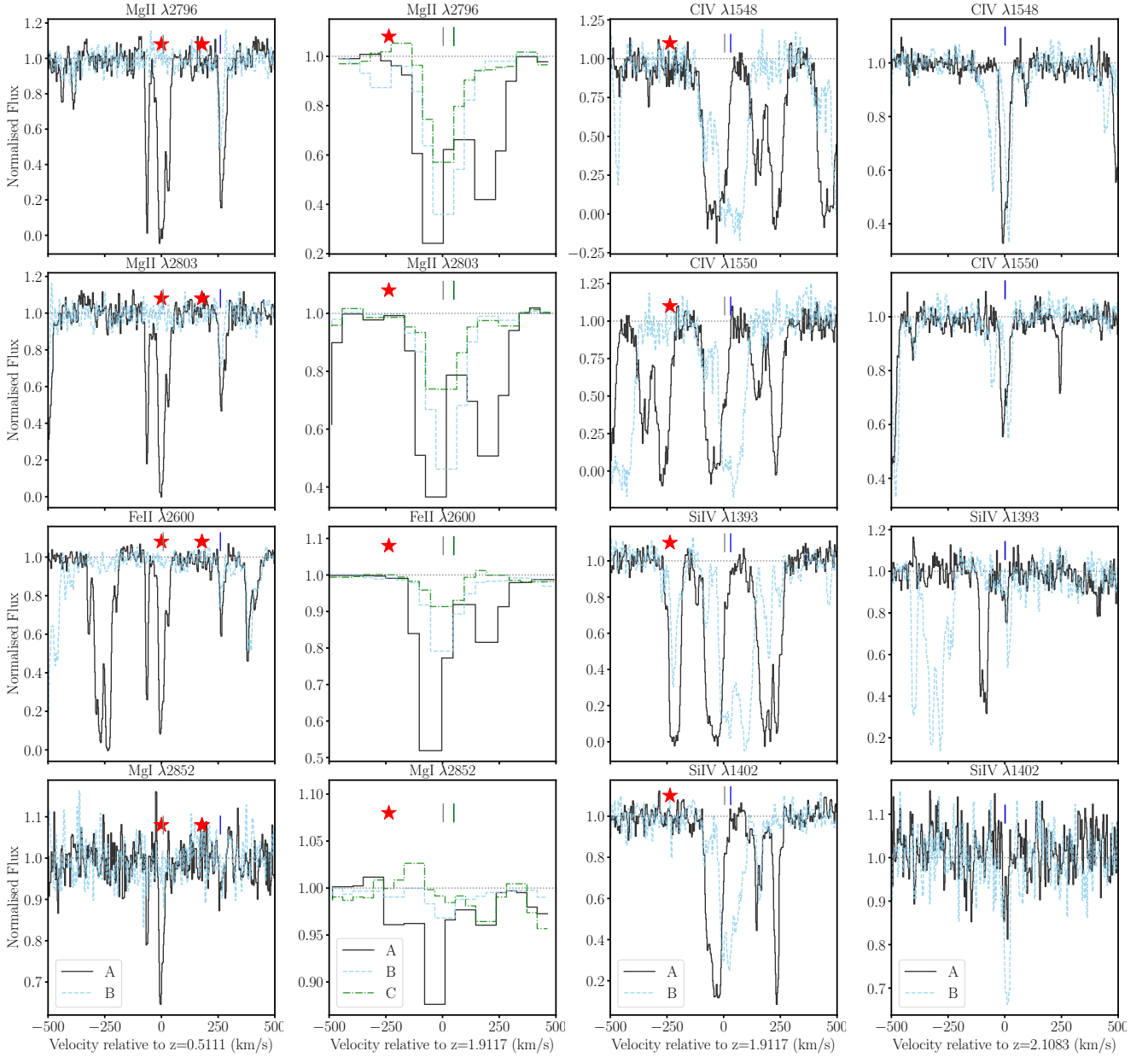


Figure 3. Examples of absorption lines detected towards the different multiple images, A, B, and C, of the quasar J1029. The corresponding ion is indicated at the top of each panel. The second column shows the normalised MUSE spectra of the multiple images A (black solid lines), B (blue dashed lines), and C (green dot-dashed lines). The other columns show the normalised UVES spectra of the quasar images A (black solid lines) and B (blue dashed lines), respectively. The optical depth-weighted median redshifts of the absorbers are marked by vertical ticks (grey for A, blue for B, green for C). The relative velocities of the galaxies identified in MUSE are marked by red stars.

the observed number density of Mg II and C IV absorbers (Mathes et al. 2017; Hasan et al. 2020), we expect to detect at random ≈ 0.6 Mg II and ≈ 1.4 C IV absorber pairs, respectively, across two quasar sightlines.

To quantify the variation in absorption across two different sightlines (X and Y), we estimate the fractional difference in the rest-frame equivalent width for each absorber pair as,

$$\Delta W_r = (W_r^X - W_r^Y) / W_r^X, \quad (1)$$

where $W_r^X > W_r^Y$. In case of non-detection in one of the sightlines,

we estimate the 3σ upper limit on the equivalent width at the same redshift as the absorber along the other sightline, for a velocity width of 100 km s^{-1} (typical of Mg II absorbers at these redshifts; e.g. Dutta et al. 2020) using the signal-to-noise ratio.

To compute the transverse physical separation between two sightlines, we first ray-trace the positions of the quasar multiple images to the absorber redshifts using the best-fit lens models presented in Acebron et al. (2022b, Model 1) and in Acebron et al. (2022a, ES-Model). For further details on these lens models, we refer to the above papers. Using the best-fit predicted positions of the quasar multiple

images at different redshifts, we estimate the physical separation between the sightlines in the absorber plane. The uncertainties in the physical separation, at the median redshift of ≈ 1.8 of the sample, due to uncertainties in the lens modeling, range from ≈ 0.4 kpc to ≈ 1 kpc with an average of ≈ 0.8 kpc for J1029, and from ≈ 0.8 kpc to ≈ 4 kpc with an average of ≈ 3 kpc for J2222. The fractional difference in equivalent width as a function of the physical separation for the Mg II $\lambda 2796$, Fe II $\lambda 2600$, and C IV $\lambda 1548$ intervening absorption lines are shown in Fig. 4.

In the case of the Mg II and Fe II absorber pairs, we are able to probe over a large range of transverse physical separations, ≈ 0.4 –150 kpc, while we probe up to ≈ 25 kpc separations for the C IV absorber pairs. The fractional difference in equivalent width, ΔW_r , shows a positive correlation with the physical separation. Considering the detections, for Mg II, the Spearman rank order correlation coefficient is $r_s = 0.58$, and the probability of the correlation arising by chance or p -value = 0.007, for Fe II, $r_s = 0.55$, p -value = 0.09, and for C IV, $r_s = 0.49$, p -value = 0.04, with similar results obtained considering the limits as detections. This increasing trend of ΔW_r with physical separation indicates that, as expected, the metal absorption becomes less spatially coherent over larger separations. We highlight specifically a transition around physical separation of ≈ 10 kpc, particularly for Mg II and Fe II, beyond which the fractional difference shows a considerable drop. Based on this we suggest a coherence length scale of ≈ 10 kpc for the metal-enriched gas around galaxies.

However, as can also be seen from Fig. 4, there is a considerable scatter in ΔW_r (ΔW_r ranges from ≈ 0.08 to ≈ 0.9) over the full range of physical separations, suggesting large variations in the spatial coherence. Particularly for Mg II, we see non-detections of paired absorption over almost the full range of physical separation probed. On the contrary, C IV absorption is always detected in both sightlines, albeit we probe up to only ≈ 25 kpc in this case. On average, the high-ionization gas phase shows a slightly higher level of coherence than the low-ionization gas phase, with C IV systems showing average $\Delta W_r \approx 0.3$ compared to average $\Delta W_r \approx 0.4$ for Mg II systems, and $\Delta W_r \approx 0.5$ for Fe II systems, at a separation of less than 25 kpc.

Fig. 5 shows the fractional difference in the equivalent width of the metal absorbers as a function of the equivalent width of the stronger absorber in a pair. We do not find any significant dependence of ΔW_r on the equivalent width for Mg II, Fe II, and C IV absorbers, suggesting that coherence is independent of the absorption strength. Additionally, we do not find any significant dependence of ΔW_r on the absorber redshift. This indicates that the correlation found between metal absorption in this sample is primarily driven by the physical separation between the sightlines.

To further investigate the coherence of the metal absorption as a function of physical separation, we plot in Fig. 6 the incidence of $\Delta W_r \leq 0.5$ in three different physical separation bins, 0 – 10 kpc, 10 – 50 kpc, and 50 – 150 kpc. We consider the 3σ limits as detections for this analysis, however, the relative trends do not change if we consider only the detections. The trends also remain similar when considering variations on the separation bins and coherence levels.

Consistent with the results from Fig. 4, the incidence decreases with increasing physical separation for the Mg II, Fe II, and C IV absorbers. The drop in incidence by a factor of ≈ 2 at separations larger than 10 kpc further supports this length scale being a characteristic coherence scale. C IV absorbers show the highest incidence of coherence, with about 90 percent of absorbers having $\Delta W_r \leq 0.5$ at separations ≤ 10 kpc, and ≈ 40 percent having $\Delta W_r \leq 0.5$ over 10–50 kpc separation. This sample lacks sightline pairs that probe C IV at larger separations. Mg II absorbers exhibit a factor of two lower incidences than C IV, and a factor of two higher incidences than Fe II at

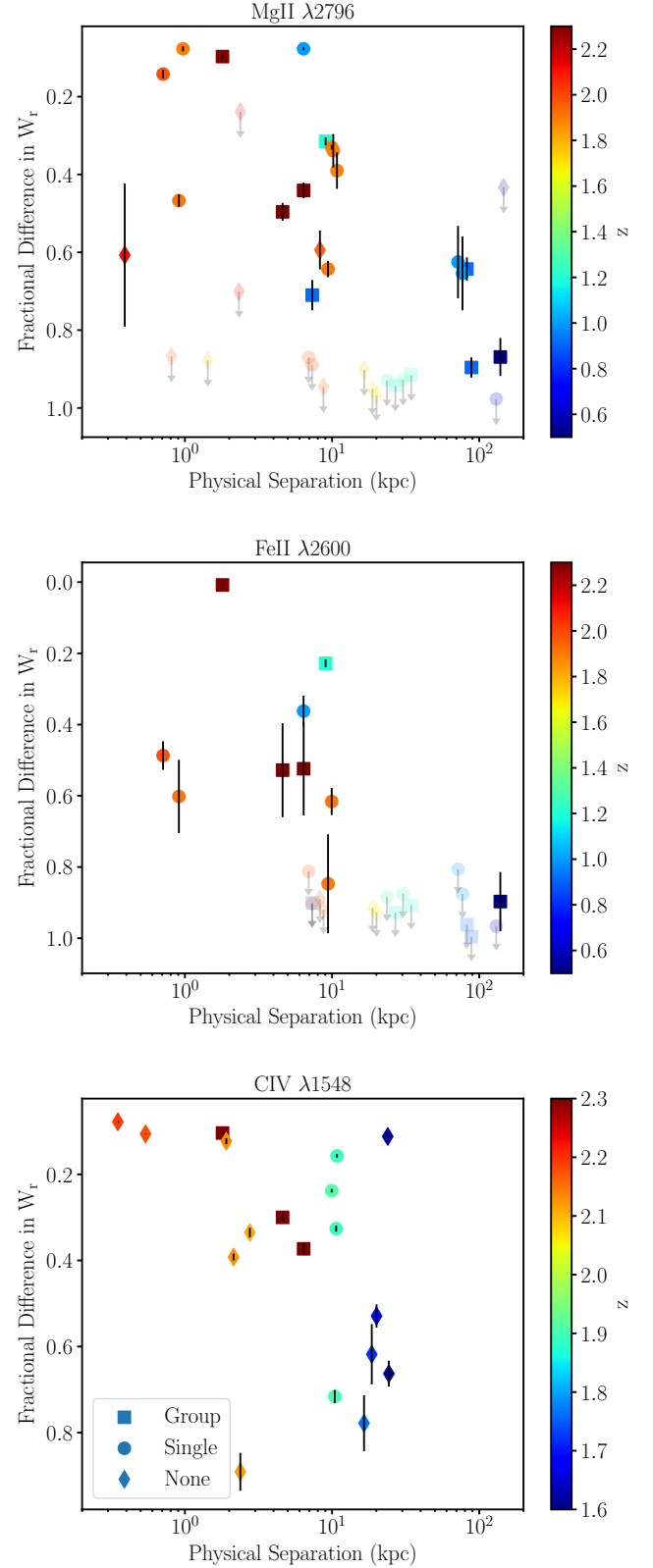


Figure 4. The fractional difference in equivalent width of Mg II (top), Fe II (centre), and C IV (bottom) absorbers as a function of physical separation between two quasar multiple images. The markers are colored by the redshift of the absorbers. Square, circle, and diamond markers indicate groups, single, and no galaxies within ± 500 km s^{-1} of the absorber redshift in the MUSE field-of-view, respectively.

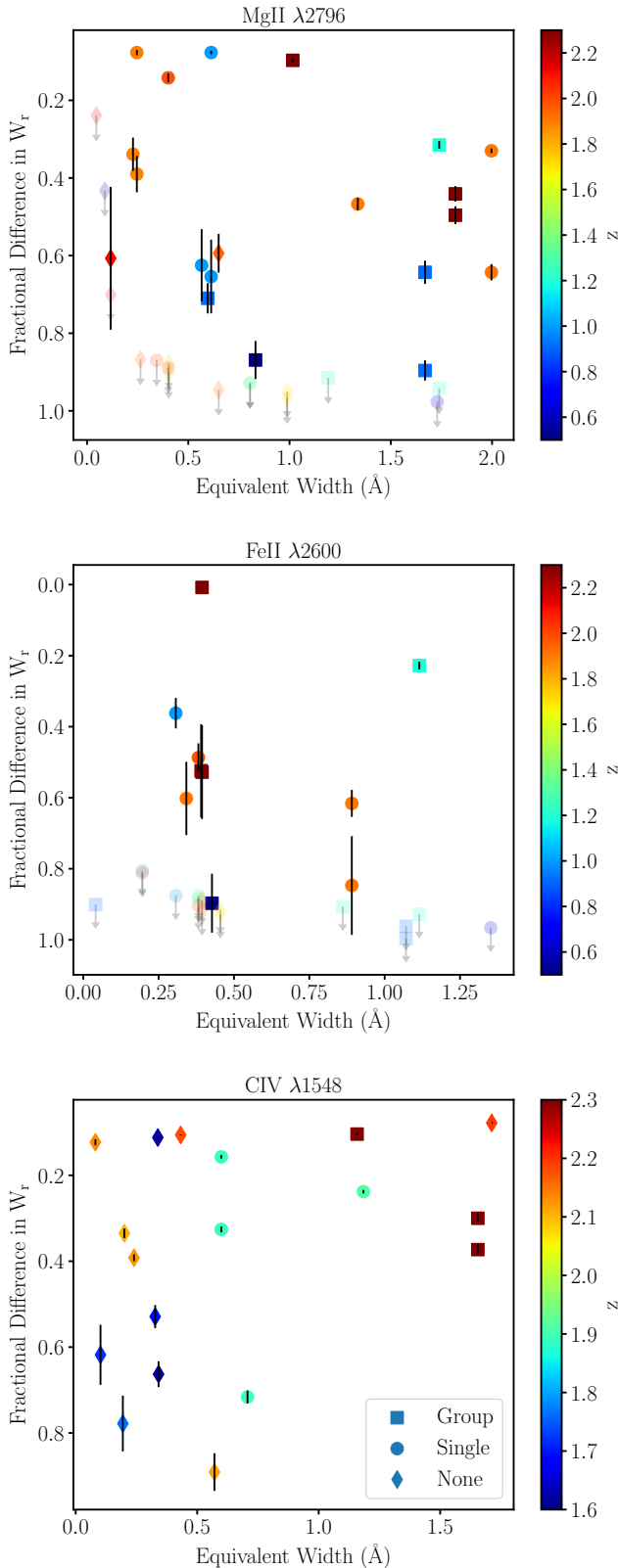


Figure 5. The fractional difference in equivalent width of Mg II (top), Fe II (centre), and C IV (bottom) absorbers as a function of the equivalent width of the stronger absorber in a pair. The symbols are the same as in Fig. 4.

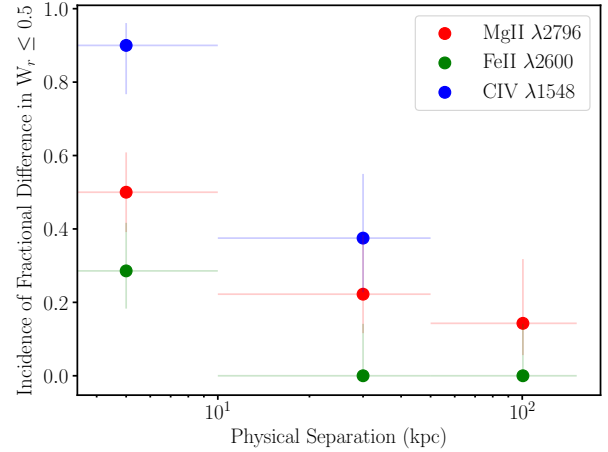


Figure 6. Incidence of fractional difference in equivalent width less than 0.5 as a function of the physical separation. Red, green, and blue markers show the incidence for Mg II, Fe II, and C IV absorbers, respectively. The vertical bars show 1σ Wilson score confidence intervals on the incidence. The range in physical separation included in each bin is shown by the horizontal bars.

separations less than 10 kpc. About 50 percent of the Mg II absorbers have $\Delta W_r \leq 0.5$ at separations ≤ 10 kpc, and the fraction drops to ≈ 22 percent at 10–50 kpc, and ≈ 14 percent at 50–150 kpc. The presence of paired Mg II absorption, even at large separations, could represent coherent structures composed of cool gas clouds extending over an area of several tens of kpc^2 . However, detailed comparison of the chemical composition and kinematic structure of the absorption is required to confirm this.

3.2 Metal absorption across three quasar sightlines

Taking advantage of the presence of three quasar multiple images in each of the fields, we next look at the coherence of metal absorption across three different sightlines. Same as when searching for paired absorption in the previous section, we search for absorbers that are detected in all three quasar sightlines within $\pm 500 \text{ km s}^{-1}$ of each other along the line-of-sight direction. We find in total five Mg II absorber triplets, two Fe II absorber triplets, and three C IV absorber triplets. For comparison, we expect to detect ≈ 0.005 and ≈ 0.03 Mg II and C IV absorber triplets, respectively, in three random quasar sightlines for the above velocity window and median redshift of the sample, based on the observed number density of Mg II and C IV absorbers (Mathes et al. 2017; Hasan et al. 2020).

Similar to the analysis in Section 3.1, we quantify the variation in absorption across the three different sightlines (X , Y , and Z) by estimating the fractional difference in equivalent width or ΔW_r for each pair of sightlines, XY , XZ , and YZ . The minimum and maximum of the ΔW_r estimates among the three pairs are plotted as a function of the corresponding physical separation in Fig. 7. Given the limited sample size, we consider ΔW_r of all three ions together for the below discussion.

If absorption of similar strength was present across all three sightlines, then the minimum and maximum ΔW_r distributions would have been similar. Instead we find that the distributions are significantly different, with the minimum ΔW_r being ≈ 0.2 on average, and the maximum ΔW_r being ≈ 0.8 on average. A two-sample Kol-

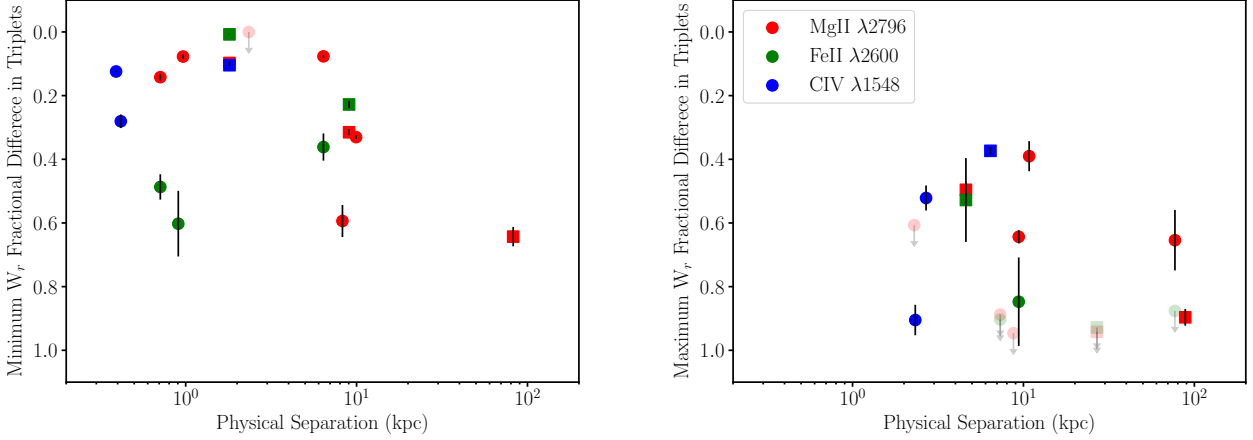


Figure 7. The minimum (left) and maximum (right) fractional difference in equivalent width of Mg II (red), Fe II (green), and C IV (blue) absorbers between two quasar multiple images in a triplet system as a function of the physical separation between the images. Square and circle markers indicate that the absorption system is associated with group and single galaxies, respectively.

mogorov–Smirnov (KS) test gives the maximum difference between the cumulative distributions of the two samples as $D = 0.8$ with a p -value of 3×10^{-5} . Moreover, the minimum ΔW_r occurs between sightlines with smaller physical separations (median of ≈ 2 kpc) compared to the maximum ΔW_r (median of ≈ 9 kpc). The distributions of the two physical separations are also different based on a KS test ($D = 0.5$, p -value = 0.01).

The above tells us that typically metal absorption of similar strength are detected across two close (≤ 10 kpc) quasar sightlines, and when detected towards a third sightline further apart, the metal absorption strength changes significantly. In other words, consistent with the results found in Section 3.1, the metal absorption becomes less coherent with increasing physical separation. Combining the minimum and maximum ΔW_r estimates, there is a clear correlation of ΔW_r with physical separation ($r_s = 0.57$, p -value = 5×10^{-4}).

3.3 Association of galaxies and metal absorption

When studying the galaxy–diffuse gas connection, the advantage of MUSE IFU data is that they allow us to simultaneously study the galaxy environment around the gas detected in absorption towards the quasar multiple images. Having investigated the coherence of metal absorption lines across the multiple quasar images, we look next at how the absorption is connected to galaxies. To do this, we search for galaxies within $\pm 500 \text{ km s}^{-1}$ of the absorber redshift in the MUSE field-of-view ($\approx 500 \times 500 \text{ kpc}^2$ at $z \approx 1$).

In Figures 4 and 5, the different markers indicate whether the absorber pair detected across two quasar sightlines is associated with a single, more than one, or no galaxies. For almost all the Mg II (90 percent) and Fe II (100 percent) absorber pairs, there is at least one galaxy counterpart detected in MUSE. About 40 and 50 percent of the Mg II and Fe II absorber pairs are associated with more than one galaxies (loosely termed as groups henceforth), respectively. For only about 40 percent of the C IV absorber pairs, we are able to identify galaxies. This is because at the redshifts of the C IV absorbers ($z \approx 1.5 - 2$) that can be detected redward of the quasar Ly α forest, it is typically challenging to identify galaxies due to the lack of strong emission lines in the optical wavelengths. When metal absorption is detected across all three quasar sightlines, we find that there is always

at least one associated galaxy, with ≈ 60 percent of the systems being associated with a single galaxy, and rest with a group of galaxies (Fig. 7).

There appears to be no significant difference between groups and single galaxies regarding the distribution of the fractional difference in the equivalent width of the associated metal absorption, albeit the sample sizes are statistically small. For the Mg II absorber pairs, which have the largest sample size, we estimate the incidence of $\Delta W_r \leq 0.5$ similar to Fig. 6, but for groups and single galaxies separately, in two physical separation bins, 0 – 10 kpc and 10 – 150 kpc. We do not find any significant difference in the incidence between Mg II absorbers associated with groups and single galaxies. However, given the small sample sizes, which hinder controlling for other parameters such as physical separation and redshift, it is difficult to derive any physical implication from the above.

Furthermore, we combined all the Mg II absorbers detected towards the different quasar multiple images and looked at how they are distributed around the associated galaxies (i.e. those within $\pm 500 \text{ km s}^{-1}$ and in the MUSE field-of-view). Fig. 8 shows the locations of the Mg II absorbers around the isolated and group galaxies, and also around the geometric centre of the groups. We again do not find any significant difference in the distribution of the Mg II absorbers around groups and single galaxies. Although, the range of physical distances probed around the single and group galaxies is quite different, making a direct comparison challenging.

4 DISCUSSION AND SUMMARY

Spectra of multiple images of strongly-lensed quasars offer the opportunity to tomographically map the foreground absorbing gas. In this work, we leverage the recent MUSE observations of two fields containing multiple images of quasars ($z \approx 2.2, 2.8$), that are strongly lensed by galaxy clusters ($z \approx 0.5, 0.6$), to study the foreground metal absorption. Thanks to the boost from the magnification effect (median magnification of the multiple quasar images $\approx 2.5 - 17$; Acebron et al. 2022b,a), the MUSE effective integration times on the multiple quasar images are some of the largest, ranging from 30 h to 1400 h, leading to signal-to-noise per pixel of $\approx 30 - 90$ around 7000 \AA in the spectra. The best-fit strong lensing models presented by Acebron

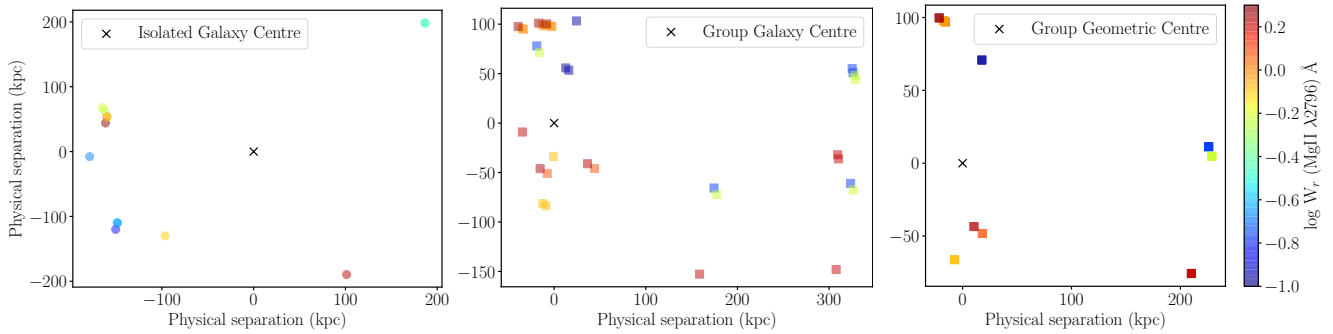


Figure 8. The locations of the Mg II absorbers around the isolated galaxies (left), group galaxies (centre), and geometric centre of the groups (right). The x and y axes are the physical separations in RA and Dec, respectively, with respect to the galaxy/group in the absorber plane. The markers are colored by the equivalent width of the Mg II absorbers.

et al. (2022b) and Acebron et al. (2022a) are used to accurately estimate the physical transverse separations between the quasar multiple images in the absorber plane. The angular separations between the quasar multiple images range from 2 to 22 arcsec, allowing us to study the low-ionization gas, traced by Mg II and Fe II absorption, over physical separations of 0.4–150 kpc at $z \approx 0.5 - 2.3$, and the high-ionization gas, traced by C IV absorption, over 0.4–25 kpc at $z \approx 1.6 - 2.3$.

By looking at how the fractional difference in rest equivalent width (ΔW_r) of the metal absorption between two quasar sightlines varies with the physical separation, we investigate the coherence of metal-enriched gas. The main results of this study are discussed below.

— Overall, ΔW_r shows an increasing trend with physical separation for both the low- and high-ionization gas phase, indicating that the metal absorption becomes less coherent on going to larger separations (Fig. 4). Within a characteristic length scale of ≈ 10 kpc, the metal-enriched gas in the CGM shows a higher level of coherence. However, there is also considerable scatter in ΔW_r , with values ranging from ≈ 0.08 to ≈ 0.9 , suggesting clumpy metal-enriched gas in the CGM even at separations smaller than coherent length scale of $\lesssim 10$ kpc. Interestingly, we find paired Mg II absorption even at ≈ 100 –150 kpc, which could be tracing the same halo. A detailed analysis of the chemical composition and kinematic structure of the absorption lines is required to check whether they trace large-scale spatially-coherent structures.

— We do not find any significant dependence of ΔW_r on the equivalent width, redshift, and associated galaxy environment, i.e., single or groups of galaxies (Fig. 5 and Fig. 8).

— Comparing the coherence of the different metal absorption, we find that C IV shows the highest degree of coherence, followed by Mg II and Fe II, implying that the coherence length of the high-ionization gas phase is likely to be larger than that of the low-ionization gas phase (Fig. 6). At separations less than 10 kpc, about 90, 50, and 30 percent of the C IV, Mg II, and Fe II absorbers have ΔW_r less than 0.5, respectively.

— Finally, we find cases of coherent metal absorption detected across three quasar sightlines, with the coherence being the highest across the closest quasar sightlines at separations $\lesssim 10$ kpc (Fig. 7).

Our results are qualitatively similar to what has been found in previous observations of metal absorption towards lensed quasars (e.g. Ellison et al. 2004; Rubin et al. 2018; Augustin et al. 2021). Based on a compilation of paired Mg II and C IV absorption towards lensed quasars in the literature, Rubin et al. (2018) reported similar increase in ΔW_r with physical separation, as well as significant scatter

in the relation, similar to what we find in this work. Consistent with our results, they find that C IV systems exhibit a higher degree of coherence than Mg II, with ≈ 90 percent of C IV systems having ΔW_r less than 0.5 at separations less than 10 kpc compared to ≈ 64 percent for Mg II. Using observations of the MUSE Ultra Deep Field, which consists of a bright quasar pair at $z \approx 3$, Fossati et al. (2019) detected a system of correlated Mg II absorption at $z \approx 0.88$ along two sightlines separated by ≈ 480 kpc that has $\Delta W_r \approx 0.68$ and is associated with a group of six galaxies. This is in line with the trends we find in this work, and supports the existence of at least some large-scale coherent structures in the cool gas.

In addition to the observational studies, a large spread in ΔW_r of Mg II absorption has been found in high resolution (≈ 0.1 kpc) FOG-GIE simulations of the CGM (Augustin et al. 2021). Further, this study found that extended inflowing filaments show coherence over larger scales than outflowing clumpy structures. Therefore, they suggest that Mg II systems that vary strongly over small scales likely trace outflowing clumps rather than filamentary structures. On the other hand, using the Illustris TNG50 simulations, Nelson et al. (2020) found that the CGM is composed of thousands of small (≈ 1 kpc) cold gas clouds that are predominantly infalling and not outflowing. Additionally, using three dimensional hydrodynamical simulations, (Fielding et al. 2020) have found evidence of a fractal nature of the cooling surface that arises within the radiative turbulent mixing layers in a multiphase medium. Further analysis of a statistical sample of galaxy haloes in high-resolution simulations is required to understand the effect of spatial resolution and different feedback models on the origin of cold gas clouds in the CGM (e.g. van de Voort et al. 2019).

A complimentary and indirect observational technique to map the distribution and extent of CGM gas has typically been to study the radial profiles of equivalent width and covering fraction in statistical ensembles of quasar-galaxy pairs. The trend of decreasing coherence of metal absorption with separation that we observe in this study is qualitatively consistent with the general decreasing trend of covering fraction of metals with projected separation from galaxies reported in the literature (e.g. Chen et al. 2010; Nielsen et al. 2013; Bordoloi et al. 2014; Dutta et al. 2020, 2021). It is interesting to note that such studies find a more extended distribution of C IV absorption than Mg II around galaxies, and increasing ionization state of the gas with increasing distance from galaxies (e.g. Werk et al. 2014; Dutta et al. 2021). Taken together with the results from this study, this could point towards a simple picture where the clumpier low-ionization gas is embedded in a more homogeneous and highly ionized gas.

Additionally, studies have found signatures of more extended Mg II absorption in overdense group-environments (e.g. Bordoloi et al. 2011; Nielsen et al. 2018; Dutta et al. 2020, 2021). Here we do not find any discernible difference in the coherence and distribution of Mg II absorption between single and groups of galaxies, with the caveat that the sample sizes are statistically small and different in properties.

In the future, a more detailed comparison of the column densities and kinematics of individual absorption components using high resolution ($R \gtrsim 20,000$) spectra would place tighter constraints on the sizes of individual gas clouds and larger-scale coherent structures, parameters that are key to constrain models of metal enrichment and mixing. Combining this with the physical properties of the galaxies obtained from the MUSE data, we can study in more detail the connection between structures of the metal-enriched CGM and the galaxy environment.

ACKNOWLEDGEMENTS

We thank the anonymous reviewer for their helpful comments. This work is based on observations collected at the European Organisation for Astronomical Research in the Southern Hemisphere under ESO programme IDs 0102.A-0642(A), 0103.A-0554(A), 092.B-0512(A). We acknowledge financial support through grants PRIN-MIUR 2017WSCC32 and 2020SKSTHZ. AA has received funding from the European Union's Horizon 2020 research and innovation programme under the Marie Skłodowska-Curie grant agreement No 101024195 - ROSEAU. This project has received funding from the European Research Council (ERC) under the European Union's Horizon 2020 research and innovation programme (grant agreement No 757535) and by Fondazione Cariplo (grant No 2018-2329).

DATA AVAILABILITY

The observational data used in this work are available from the European Southern Observatory archive: <https://archive.eso.org>.

REFERENCES

- Acebron A., et al., 2022a, *A&A*, 668, A142
 Acebron A., et al., 2022b, *ApJ*, 926, 86
 Arrigoni Battaia F., Hennawi J. F., Prochaska J. X., Oñorbe J., Farina E. P., Cantalupo S., Lusso E., 2019, *MNRAS*, 482, 3162
 Augustin R., Péroux C., Hamanowicz A., Kulkarni V., Rahmani H., Zanella A., 2021, *MNRAS*, 505, 6195
 Bacon R., et al., 2010, in McLean I. S., Ramsay S. K., Takami H., eds, Society of Photo-Optical Instrumentation Engineers (SPIE) Conference Series Vol. 7735, Ground-based and Airborne Instrumentation for Astronomy III. p. 773508, doi:10.1117/12.856027
 Bertin E., Arnouts S., 1996, *A&AS*, 117, 393
 Bordoloi R., et al., 2011, *ApJ*, 743, 10
 Bordoloi R., et al., 2014, *ApJ*, 796, 136
 Borisova E., et al., 2016, *ApJ*, 831, 39
 Burchett J. N., Rubin K. H. R., Prochaska J. X., Coil A. L., Vaught R. R., Hennawi J. F., 2021, *ApJ*, 909, 151
 Chen H.-W., Wild V., Tinker J. L., Gauthier J.-R., Helsby J. E., Shectman S. A., Thompson I. B., 2010, *ApJ*, 724, L176
 Chen H.-W., Gauthier J.-R., Sharon K., Johnson S. D., Nair P., Liang C. J., 2014, *MNRAS*, 438, 1435
 Dutta R., et al., 2020, *MNRAS*, 499, 5022
 Dutta R., et al., 2021, *MNRAS*, 508, 4573

- Dutta R., et al., 2023, *MNRAS*, 522, 535
 Ellison S. L., Ibata R., Pettini M., Lewis G. F., Aracil B., Petitjean P., Srianand R., 2004, *A&A*, 414, 79
 Fielding D. B., Ostriker E. C., Bryan G. L., Jermyn A. S., 2020, *ApJ*, 894, L24
 Fossati M., et al., 2019, *MNRAS*, 490, 1451
 Fossati M., et al., 2021, *MNRAS*, 503, 3044
 Fumagalli M., O'Meara J. M., Prochaska J. X., 2016, *MNRAS*, 455, 4100
 Galbiati M., Fumagalli M., Fossati M., Lofthouse E. K., Dutta R., Prochaska J. X., Murphy M. T., Cantalupo S., 2023, *MNRAS*, 524, 3474
 Haislmaier K. J., Tripp T. M., Katz N., Prochaska J. X., Burchett J. N., O'Meara J. M., Werk J. K., 2021, *MNRAS*, 502, 4993
 Hasan F., et al., 2020, *ApJ*, 904, 44
 Hennawi J. F., Prochaska J. X., 2007, *ApJ*, 655, 735
 Kulkarni V. P., Cashman F. H., Lopez S., Ellison S. L., Som D., Maureira M. J., 2019, *ApJ*, 886, 83
 Leclercq F., et al., 2017, *A&A*, 608, A8
 Leclercq F., et al., 2022, *A&A*, 663, A11
 Lofthouse E. K., et al., 2023, *MNRAS*, 518, 305
 Lopez S., et al., 2018, *Nature*, 554, 493
 Martin C. L., Scannapieco E., Ellison S. L., Hennawi J. F., Djorgovski S. G., Fournier A. P., 2010, *ApJ*, 721, 174
 Mathes N. L., Churchill C. W., Murphy M. T., 2017, *arXiv e-prints*, p. arXiv:1701.05624
 Mintz A., et al., 2022, *AJ*, 164, 51
 Nelson D., et al., 2020, *MNRAS*, 498, 2391
 Nielsen N. M., Churchill C. W., Kacprzak G. G., 2013, *ApJ*, 776, 115
 Nielsen N. M., Kacprzak G. G., Pointon S. K., Churchill C. W., Murphy M. T., 2018, *ApJ*, 869, 153
 Oguri M., et al., 2013, *MNRAS*, 429, 482
 Péroux C., Howk J. C., 2020, *ARA&A*, 58, 363
 Péroux C., Rahmani H., Arrigoni Battaia F., Augustin R., 2018, *MNRAS*, 479, L50
 Rauch M., Sargent W. L. W., Barlow T. A., 2001, *ApJ*, 554, 823
 Rubin K. H. R., Hennawi J. F., Prochaska J. X., Simcoe R. A., Myers A., Lau M. W., 2015, *ApJ*, 808, 38
 Rubin K. H. R., et al., 2018, *ApJ*, 859, 146
 Sameer et al., 2021, *MNRAS*, 501, 2112
 Sharon K., et al., 2017, *ApJ*, 835, 5
 Soto K. T., Lilly S. J., Bacon R., Richard J., Conseil S., 2016, *MNRAS*, 458, 3210
 Tejos N., et al., 2021, *MNRAS*, 507, 663
 Tumlinson J., et al., 2011, *Science*, 334, 948
 Tumlinson J., Peebles M. S., Werk J. K., 2017, *ARA&A*, 55, 389
 Turner M. L., Schaye J., Steidel C. C., Rudie G. C., Strom A. L., 2014, *MNRAS*, 445, 794
 Weilbacher P. M., et al., 2020, *A&A*, 641, A28
 Werk J. K., et al., 2014, *ApJ*, 792, 8
 Zabl J., et al., 2021, *MNRAS*, 507, 4294
 Zahedy F. S., Chen H.-W., Rauch M., Wilson M. L., Zabludoff A., 2016, *MNRAS*, 458, 2423
 Zahedy F. S., et al., 2021, *MNRAS*, 506, 877
 van de Voort F., Springel V., Mandelker N., van den Bosch F. C., Pakmor R., 2019, *MNRAS*, 482, L85

APPENDIX A: METAL ABSORPTION LINES DETECTED TOWARDS THE QUASAR MULTIPLE IMAGES

This paper has been typeset from a $\text{\TeX}/\text{\LaTeX}$ file prepared by the author.

Table A1. List of Mg II and C IV systems detected towards image A of J1029.

Ion	Rest Wavelength (\AA)	Redshift	Equivalent Width (W_r ; \AA)	Error in W_r (\AA)
MgII	2796	0.5111	0.832	0.011
MgII	2803		0.635	0.012
MgI	2852		0.114	0.012
FeII	2600		0.427	0.008
MgII	2796	0.9186	1.669	0.008
MgII	2803		1.461	0.009
MgI	2852		0.395	0.010
FeII	2600		1.071	0.007
MgII	2796	1.0059	0.212	0.030
MgII	2803		0.094	0.017
MgII	2796	1.6931	0.988	0.021
MgII	2803		0.715	0.021
MgI	2852		0.064	0.020
FeII	2600		0.455	0.014
MgII	2796	1.8912	0.150	0.016
MgII	2803		0.083	0.015
MgII	2796	1.9117	1.997	0.019
MgII	2803		1.749	0.019
MgI	2852		0.186	0.019
FeII	2600		0.891	0.024
MgII	2796	1.9417	0.650	0.019
MgII	2803		0.402	0.015
MgI	2852		0.069	0.014
FeII	2600		0.394	0.017
CIV	1548	1.6150	0.341	0.005
CIV	1550		0.324	0.006
SiIV	1393		0.105	0.006
SiIV	1402		0.074	0.006
CIV	1548	1.6228	0.338	0.005
CIV	1550		0.185	0.005
CIV	1548	1.6930	0.327	0.008
CIV	1550		0.155	0.009
CIV	1548	1.7210	0.102	0.005
CIV	1550		0.047	0.005
CIV	1548	1.7651	0.043	0.003
CIV	1550		0.031	0.003
CIV	1548	1.8908	0.505	0.009
CIV	1550		0.466	0.008
SiIV	1393		0.182	0.003
SiIV	1402		0.272	0.003
CIV	1548	1.8947	0.404	0.005
CIV	1550		0.333	0.005
CIV	1548	1.8981	0.201	0.004
CIV	1550		0.152	0.006
SiIV	1393		0.020	0.003
SiIV	1402		0.011	0.003
CIV	1548	1.9117	1.184	0.014
CIV	1550		0.884	0.015
SiIV	1393		0.882	0.008
SiIV	1402		0.492	0.008
CIV	1548	2.1083	0.133	0.003
CIV	1550		0.080	0.003
SiIV	1393		0.025	0.003
SiIV	1402		0.013	0.003
CIV	1548	2.1195	0.062	0.003
CIV	1550		0.030	0.003
CIV	1548	2.1269	0.146	0.002
CIV	1550		0.108	0.002
CIV	1548	2.1349	0.081	0.003
CIV	1550		0.043	0.003
CIV	1548	2.1819	0.432	0.004
CIV	1550		0.301	0.004
SiIV	1393		0.112	0.007
SiIV	1402		0.059	0.006
CIV	1548	2.1954	1.712	0.004
CIV	1550		1.313	0.004

Table A2. List of Mg II and C IV systems detected towards image B of J1029.

Ion	Rest Wavelength (\AA)	Redshift	Equivalent Width (W_r ; \AA)	Error in W_r (\AA)
MgII	2796	0.5124	0.109	0.006
MgII	2803		0.053	0.006
FeII	2600		0.044	0.004
MgII	2796	0.5654	0.088	0.009
MgII	2803		0.038	0.008
MgII	2796	0.6731	1.729	0.010
MgII	2803		1.585	0.010
MgI	2852		0.612	0.010
FeII	2600		1.352	0.011
MgII	2796	0.9184	0.173	0.005
MgII	2803		0.103	0.006
FeII	2600		0.004	0.003
MgII	2796	1.0032	0.613	0.020
MgII	2803		0.441	0.020
MgI	2852		0.044	0.006
FeII	2600		0.307	0.004
MgII	2796	1.7628	0.404	0.014
MgII	2803		0.412	0.012
MgI	2852		0.055	0.010
MgII	2796	1.8939	0.246	0.014
MgII	2803		0.427	0.013
MgII	2796	1.9122	1.337	0.020
MgII	2803		0.926	0.020
MgI	2852		0.051	0.013
FeII	2600		0.342	0.019
MgII	2796	1.9788	0.401	0.019
MgII	2803		0.299	0.018
MgI	2852		0.035	0.013
FeII	2600		0.382	0.011
CIV	1548	1.6085	0.040	0.003
CIV	1550		0.028	0.003
CIV	1548	1.6150	0.115	0.005
CIV	1550		0.138	0.007
CIV	1548	1.6221	0.300	0.003
CIV	1550		0.158	0.004
CIV	1548	1.6253	0.024	0.003
CIV	1550		0.012	0.003
CIV	1548	1.6556	0.172	0.006
CIV	1550		0.093	0.006
CIV	1548	1.6924	0.154	0.007
CIV	1550		0.057	0.004
CIV	1548	1.7065	0.050	0.003
CIV	1550		0.025	0.003
CIV	1548	1.7211	0.039	0.004
CIV	1550		0.020	0.004
CIV	1548	1.7626	0.194	0.009
CIV	1550		0.112	0.009
CIV	1548	1.8910	0.599	0.010
CIV	1550		0.683	0.008
SiIV	1393		0.138	0.005
SiIV	1402		0.134	0.005
CIV	1548	1.8943	0.707	0.005
CIV	1550		0.689	0.007
SiIV	1393		0.468	0.009
SiIV	1402		0.425	0.009
CIV	1548	1.9017	0.559	0.007
CIV	1550		0.387	0.008
SiIV	1393		0.200	0.005
SiIV	1402		0.159	0.005
CIV	1548	1.9120	0.902	0.010
CIV	1550		0.719	0.011
SiIV	1393		0.688	0.006
SiIV	1402		0.346	0.006
CIV	1548	2.1083	0.200	0.005
CIV	1550		0.106	0.005
SiIV	1393		0.036	0.003
SiIV	1402		0.051	0.004

Table A3. List of Mg II and C IV systems detected towards image B of J1029 (continued from Table A2).

Ion	Rest Wavelength (Å)	Redshift	Equivalent Width (W_r ; Å)	Error in W_r (Å)
CIV	1548	2.1209	0.571	0.004
CIV	1550		0.504	0.004
MgII	2796		0.046	0.012
MgII	2803		0.025	0.011
CIV	1548	2.1285	0.240	0.004
CIV	1550		0.182	0.004
SiIV	1393		0.050	0.004
SiIV	1402		0.021	0.004
CIV	1548	2.1349	0.071	0.003
CIV	1550		0.031	0.003
CIV	1548	2.1820	0.386	0.004
CIV	1550		0.234	0.004
SiIV	1393		0.144	0.006
SiIV	1402		0.093	0.006
CIV	1548	2.1955	1.579	0.004
CIV	1550		1.236	0.004

Table A4. List of Mg II and C IV systems detected towards image C of J1029.

Ion	Rest Wavelength (Å)	Redshift	Equivalent Width (W_r ; Å)	Error in W_r (Å)
MgII	2796	0.9182	0.596	0.028
MgII	2803		0.267	0.022
MgII	2796	1.0032	0.566	0.025
MgII	2803		0.425	0.025
MgI	2852		0.140	0.029
FeII	2600		0.196	0.023
MgII	2796	1.8939	0.227	0.016
MgII	2803		0.221	0.015
MgII	2796	1.9122	0.712	0.022
MgII	2803		0.521	0.023
FeII	2600		0.136	0.022
MgII	2796	1.9417	0.264	0.021
MgII	2803		0.085	0.016
MgII	2796	1.9788	0.344	0.020
MgII	2803		0.277	0.030
MgI	2852		0.097	0.022
FeII	2600		0.196	0.015
CIV	1548	2.1077	0.278	0.020
CIV	1550		0.156	0.016
CIV	1548	2.1206	0.652	0.014
CIV	1550		0.688	0.017
MgII	2796		0.117	0.018
MgII	2803		0.082	0.015
CIV	1548	2.1957	1.576	0.007
CIV	1550		1.166	0.007

Table A5. List of Mg II and C IV systems detected towards image A of J2222.

Ion	Rest Wavelength (Å)	Redshift	Equivalent Width (W_r ; Å)	Error in W_r (Å)
MgII	2796	1.2017	1.191	0.030
MgII	2803		1.154	0.036
MgI	2852		0.410	0.029
FeII	2600		0.861	0.033
MgII	2796	2.2981	1.016	0.034
MgII	2803		1.110	0.029
FeII	2600		0.391	0.023
CIV	1548		1.037	0.023
CIV	1550		1.081	0.020
CIV	1548	2.8022	1.155	0.014
CIV	1550		0.912	0.011
SiIV	1393		0.503	0.020
SiIV	1402		0.230	0.015

Table A6. List of Mg II and C IV systems detected towards image B of J2222.

Ion	Rest Wavelength (Å)	Redshift	Equivalent Width (W_r ; Å)	Error in W_r (Å)
MgII	2796	1.2017	1.739	0.030
MgII	2803		1.556	0.026
MgI	2852		0.597	0.032
FeII	2600		1.115	0.036
MgII	2796	2.2985	0.917	0.032
MgII	2803		1.105	0.031
FeII	2600		0.394	0.024
CIV	1548		1.158	0.023
CIV	1550		1.608	0.023
CIV	1548	2.8022	1.102	0.012
CIV	1550		0.904	0.014
SiIV	1393		0.482	0.019
SiIV	1402		0.257	0.017

Table A7. List of Mg II and C IV systems detected towards image C of J2222.

Ion	Rest Wavelength (Å)	Redshift	Equivalent Width (W_r ; Å)	Error in W_r (Å)
MgII	2796	1.2965	0.805	0.041
MgII	2803		0.622	0.043
MgI	2852		0.291	0.044
FeII	2600		0.382	0.029
MgII	2796	2.2990	1.819	0.055
MgII	2803		1.856	0.050
FeII	2600		0.186	0.045
CIV	1548		1.655	0.038
CIV	1550		1.677	0.035
CIV	1548	2.8022	1.082	0.012
CIV	1550		0.858	0.014
SiIV	1393		0.507	0.031
SiIV	1402		0.191	0.025